ENGINEERING

Addressing gain-bandwidth trade-off by a monolithically integrated photovoltaic transistor

Yuanzhe Li[1], Guowei Chen[2], Shenghe Zhao[1], Chuan Liu[2]*, Ni Zhao[1]*

Copyright © 2022 The Authors, some rights reserved; exclusive licensee American Association for the Advancement of Science. No claim to original U.S. Government Works. Distributed under a Creative Commons Attribution NonCommercial License 4.0 (CC BY-NC).

The gain-bandwidth trade-off limits the development of high-performance photodetectors; i.e., the mutual restraint between the response speed and gain has intrinsically limited performance optimization of photomultiplication phototransistors and photodiodes. Here, we show that a monolithically integrated photovoltaic transistor can solve this dilemma. In this structure, the photovoltage generated by the superimposed perovskite solar cell, acting as a float gate, is amplified by the underlying metal oxide field-effect transistor. By eliminating deep-trap defects through processing optimization, we achieved devices with a maximum responsivity close to 6×10^4 A/W, a specific detectivity (D^*) of 1.06×10^{13} Jones, and an f_{3dB} of 1.2 MHz at a low driving voltage of 3 V. As a result, a record gain-bandwidth product is achieved. The device further exhibits the advantage in photoplethysmography detection with weak illuminations, where our device accurately detects the detailed features that are out of the capability of conventional photodetectors.

INTRODUCTION

High-performance photodetectors are essential for applications such as imaging (*1*), optical communications (*2*), and biomedical monitoring (*3*). An ideal photodetector should simultaneously have high gain, fast response, and low power consumption. So far, most photodetectors have been designed on the basis of photoconductivity, collecting photoelectrons in the form of electric current. However, the biggest disadvantage of this design is that it cannot support fast response and large current gain at the same time. For instance, a typical photomultiplication phototransistor (PT) can provide a responsivity (R) of more than 10^5 A/W when a 3-dB bandwidth (f_{3dB}) is less than 100 Hz (*4*) Meanwhile, f_{3dB} of a typical photodiode (PD) can be close to 35 MHz, but the responsivity is less than 1 A/W (*5*).

One possible solution to this dilemma is a photovoltaic transistor (PVT) containing two modules: photovoltaic (PV) and field-effect transistor (FET). The key to such structure is to spatially separate the sensing and gain mechanisms, with the PV module responsible for providing a photovoltage upon light excitation and the FET module outputting an electrical signal with amplification. Early works mainly use linear PV relationships. Liu and Luryi (*6*) proposed a PVT structure by stacking asymmetric semiconductor superlattice on a Si FET. When the minority carrier lifetime is sufficiently short, the internal polarization in the superlattice can generate a photovoltage linear to light intensity. However, similar to other devices relying on linear relationships, the signal of this PVT is poor under low-light illumination. Another strategy is to use logarithmic PV relationships, which is frequently adopted in recent works. Adinolfi and Sargent (*7*) fabricated a PVT device using a rectifying heterojunction formed by colloidal quantum dots (CQDs) and a silicon active layer. Compared to the planar structure by simply connecting PV and FET modules via conducting wires (*8*), the monolithic vertical structure minimizes resistor-capacitor (RC) time constant and increases the response speed. The photovoltage generated by the CQD/Si interface together with the high transconductance of the silicon transistor results in a responsivity of more than 10^4 A/W and an f_{3dB} of around 100 kHz. The performance under low light intensity is also greatly enhanced, attributed to the logarithmic light intensity–photovoltage relationship. However, in practice, a high-performance CQD/Si heterojunction is difficult to form, because silicon can be quickly oxidized or contaminated during solution deposition of the CQD layer, preventing the formation of the built-in field at the heterojunction.

Here, we propose and demonstrate a back-illuminated PVT structure, where a solar cell is monolithically built on a transparent FET, with its cathode and anode serving as the control gate and floating gate, respectively, of the FET. Specifically, we select indium gallium zinc oxide (IGZO) as the active material of the FET for its high transparency in a visible–near-infrared (NIR) window (*9*), high mobility (*10*), low-processing temperature (thus compatibility with flexible substrates) (*11*), and good chemical resistance to organic solvents (*9*). For the solar cell, we select perovskite as the light absorber. Perovskite solar cells can be low-temperature processed (*12*), thus minimizing the damage to the underlying FET while at the same time providing superior PV performances, e.g., a large open-circuit voltage (V_{OC}) and a high power conversion efficiency of up to 25.5% (*13*–*15*). Similar to organic and dye-sensitized solar cells, perovskite solar cells operate particularly efficiently under low-light illumination (*16*, *17*), where commercial silicon solar cells become insufficient (*18*, *19*).

We first theoretically illustrate the advantage of the PVT structure in maintaining high gain and large frequency at weak light intensity. To obtain the predicted photodetection performance, we then optimize the perovskite-absorbing layer with additive modification and surface passivation to remove deep trap states, thus enabling high V_{OC} even at low light intensity and fast response speed (a rise time of 420 ns and a fall time of 3.3 μs). As a result, the PVT device demonstrates a maximum responsivity close to 6×10^4A/W, a specific detectivity (D^*) of 1.06×10^{13} Jones, and an f_{3dB} of 1.2 MHz

[1]Department of Electronic Engineering, The Chinese University of Hong Kong, Shatin, New Territories, Hong Kong SAR 999077, China. [2]The State Key Laboratory of Optoelectronic Materials and Technologies and the Guangdong Province Key Laboratory of Display Material and Techology, School of Electronics and Information Technology, Sun Yat-sen University, Guangzhou 510275, China.
*Corresponding author. Email: nzhao@ee.cuhk.edu.hk (N.Z.); liuchuan5@mail.sysu.edu.cn (C.L.)

at a low driving voltage of 3 V. By comparing our PVT with a conventional PT in tracking photoplethysmogram (PPG) signals on fingertips, we demonstrate the unique advantage of the PVT in preserving signal fidelity in weak light applications.

RESULTS

Device structure and operation model

The structure of our PVT device is illustrated in Fig. 1A. Because of the n-type nature of IGZO, an inverted PV cell structure is adopted so that the generation of a positive photovoltage at the indium tin oxide (ITO) anode (serving also as the floating gate of the FET) can trigger the accumulation of electrons in the n-channel and consequently result in an amplified current flow. The control gate modulation is achieved by applying an external bias voltage on the cathode of the solar cell while keeping the source electrode of the FET grounded. When used for photodetection, a control gate voltage V_G is applied to set the work regime for the PVT and a channel voltage V_D is used to read out the current signal.

To quantitatively analyze how the PVT structure could address the widely seen gain-frequency trade-off in photoconductivity-based photodetectors, we compare the PVT and two other common photodetector structures, i.e., PT and PD, in terms of responsivity and bandwidth, which are arguably the two most important figures of merit of photodetectors.

Devices with ohmic contact are discussed here for simplicity. The key process and physical quantities for gain or amplification, which determines responsivity, are distinct (illustrated in Fig. 1B): (i) For a PVT, the photogenerated *e-h* pairs in the PV cell separate the quasi-Fermi energy E_{Fn} and E_{Fp} and build up $V_{oc} = E_g/q + kT\ln(\text{EQE})/q$, where E_g is the bandgap, q is the elementary charge, kT is the thermal energy, and the external quantum efficiency EQE can be determined by the density of *e-h* pairs (*20*). The built-in V_{OC} is imposed on the control gate V_G and modulates the drain current I_D, generating electrical gain. [Note that the PVT is still a three-terminal (i.e., source, drain, and gate terminals) device. Here, we separate the device structure into a PV module and a FET module to help illustrate the device operation mechanism.] (ii) For a PT (e.g., n-type), photogenerated holes electrostatically induce extra electrons, i.e., equivalently shifting threshold voltage V_{th} toward negative, giving the photoelectrical gain. The differential of time for concentration of excess holes (Δp, cm^{-3}) is simplified as $d\Delta p/dt = G - \Delta p/\tau$, where G is the average generation rate of *e-h* pairs ($\text{cm}^{-3}\ \text{s}^{-1}$). The Δp at transient and steady state is $\Delta p(t) = G\tau[1 - \exp(-t/\tau_p)]$ and $\Delta p(\infty) = G\tau_p$, respectively. The extra electrons causing ΔV_{th} are induced by Δp with the concentration per unit area as $\Delta p\lambda_{sc}$, where λ_{sc} is the effective thickness (i.e., penetration depth of the light) of the semiconductor channel. (iii) For a PD, as the transit time τ_t within which carriers are swept out of the semiconductor is usually shorter than the recombination lifetime τ (*21*), the photocurrent increment as the photogain is $\Delta J = qGd$, rather than $\Delta J = qG\tau(\mu_n + \mu_p)\epsilon$ as in an extra thick PD or long photoconductor, where μ_n, μ_p, and ϵ represent electron mobility, hole mobility, and drift electric field, respectively. The relations between the key physical quantities with the illumination power P are summarized as follows

$$V_{OC} = \frac{E_g}{q} + \frac{kT}{\alpha q}\ln\frac{np}{N_c^2} \propto \ln P \quad (1)$$

$$\Delta V_{th} = \frac{q\Delta p}{C_i} \approx \frac{q\lambda_{sc}}{C_i}\tau_p G \propto \tau_p P^{\beta} \quad (2)$$

$$\Delta J = qGd \propto P^{\gamma} \quad (3)$$

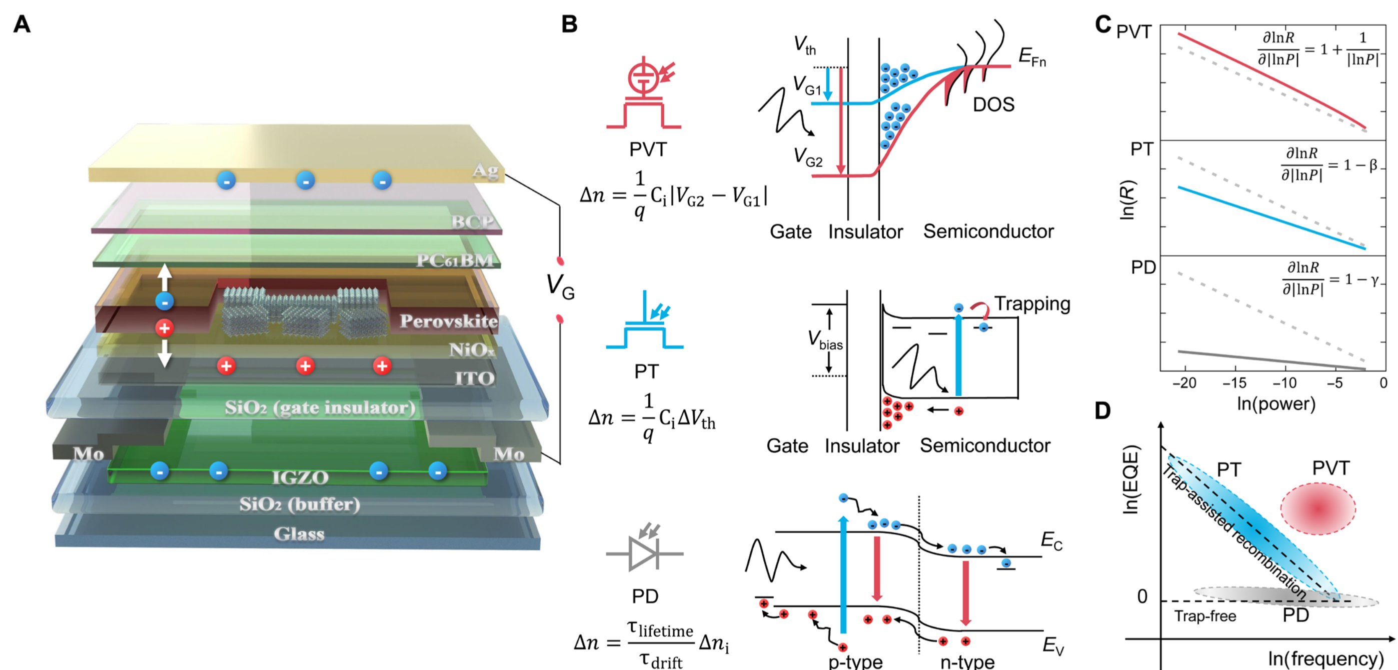

Fig. 1. Working principle of a PVT. (**A**) A scheme of PVT structure and working principle. (**B**) Comparison between working principles of different types of photodetectors. DOS, density of states. (**C**) Comparison of the responsivity (*R*)–power relationship of different types of devices, where the dashed lines denote the slope of 1. (**D**) Illustration of EQE-frequency relations for the PVT, PT, and PD.

Here, n, p, and N_C are the electron density, hole density, and effective density of conduction band, respectively; C_i is gate dielectric capacitance per unit area; τ_p is the recombination lifetime for minority carriers; and d is the transit length for carriers, i.e., the thickness or length of a PD or photoconductor. Constant terms α, β, and γ are used here to simplify the equations, with $1 \le \alpha \le 2$ depending on whether the monomolecular (Shockley-Read-Hall) recombination or bimolecular (Langevin) recombination dominates; $\beta \le 1$ and $\gamma \le 1$ are related to generation and recombination processes, where $\beta \ll 1$ has been found in PT and $\gamma \sim 1$ has been found in defectless PD (i.e., 100% EQE) (*21*). For most of the PD with low defect density, γ is also close to 1. The corresponding responsivity $R = (I_{ph} - I_{dark})/P$ is then

$$R_{PVT} = \frac{g_m V_{OC}}{P} \propto \frac{g_m |\ln P|}{P} \quad (4)$$

$$R_{PT} = \frac{g_m \Delta V_{th}}{P} \propto \frac{g_m \tau_p}{P^{1-\beta}} \quad (5)$$

$$R_{PD} = \frac{(I_{ph} - I_{dark})}{P} \propto \frac{I_0}{P^{1-\gamma}} \quad (6)$$

Here, $g_m = \partial I_d / \partial V_g \approx V_G W C_i \mu_{eff} / L$ is the transconductance in the saturated regime of the transistor, with W and L as the channel width and length, respectively, and μ_{eff} as the effective carrier mobility including the effect of contact resistance. For instance, μ_{eff} can be expressed as: $\mu_{eff} = \mu_0/[1 + \mu_0 R_C W C_i (V_G - V_{th} - V_D/2)/L]$ (*22–24*), where R_C is the sum of the source and drain contact resistances and μ_0 is the intrinsic channel mobility (i.e., the carrier mobility in the absence of any contact resistance). This is suitable for both PVT and PT devices. This set of equations predicts two trends for responsivity (Fig. 1C): (i) R_{PVT} and R_{PT} increase substantially with decreasing P, whereas R_{PD} remains almost unchanged for most of the PDs (for PDs with a high density of deep traps, the slope is nonzero) (*25*); (ii) the $R_{PVT} - P$ slope is steeper than the $R_{PT} - P$ slope, suggesting that the PVT could be very suitable for weak-light detection. According to Eq. 4, the large R_{PVT} calls for a solar cell with large power conversion efficiency and a transistor with large g_m.

The switching speed for PVT can be approximated by $f \approx 1/(\tau_{PV} + \tau_{TFT})$, where the photovoltage cell delay τ_{PV} is determined by the recombination rate and the transistor gate delay is $\tau_{TFT} = CV/I$. A detailed derivation of the frequency response is included in the Supplementary Materials (fig. S1). The R and f can be optimized independently in PVT. In comparison, large R in PD and PT is typically induced by traps as $R_{PT} \propto \tau_p$. One type of excess carriers (often minorities) may become localized via the trapping effect of defects, surface states, and surface depletion region (*21*), while the other type can keep transporting in a circuit until the localized ones are thermally or light-activated (detrapping) for the thereafter recombination. Such a process can substantially enhance R but lead to a slow recovery speed and even photopersistent current in transistors. The R and f_{3dB} for different ohmic contact devices are illustrated in Fig. 1D. Note that the vertically integrated structure avoids the interconnects and parasitic capacitance typically present in the lateral integration and therefore reduces RC delay of the device. Hence, the monolithic PVT integrates the advantages of large R in weak illumination, the ease for enhancing switching speed, and the small device footprint.

Optimization of PV module

According to the theoretical device model, a large V_{OC} will result in a high responsivity. Therefore, we first seek to minimize the nonradiative recombination processes in the PV cell by minimizing the bulk and surface defects of the perovskite layer (*26*). In this study, mixed cesium (Cs)–formamidinium (FA) triiodide perovskite $Cs_{0.07}FA_{0.93}PbI_3$ is chosen as the absorbing layer for its wide absorption window of up to the 800-nm NIR range (*27*, *28*), which is critical for biomedical applications. (We note that a higher V_{OC} can be obtained by enlarging the bandgap of the perovskite but that would narrow the NIR detection range.) The crystal structure, optical absorption spectrum, and morphology of the perovskite film are shown in Fig. 2 (A to C, respectively). It can be seen that the pristine film exhibits moderate crystallinity with visible surface segregates.

To improve the film crystallinity and morphology, we combined the use of a precursor additive, cyclohexylmethyl amine (Cy), and post-deposition treatment by phenethylammonium iodide (PEAI) (see details of the processing conditions in Materials and Methods). Cy has previously been used to generate air-stable two-dimensional (2D) perovskites and shown to promote the directional growth of crystal grains (*29*). Here, to avoid the generation of 2D phases, which may lower the efficiency of the PV cell, while leveraging the capability of Cy in promoting crystal growth and moisture resistance, we introduced only a small amount of Cy in the perovskite precursor solution (1 n/n% relative to PbI_2). As shown in Fig. 2A, the crystallinity of the perovskite film is greatly enhanced after the addition of Cy. Furthermore, the grain homogeneity of the perovskite film has also been improved as shown in the scanning electron microscopy (SEM) images in Fig. 2 (C and D) and fig. S2A. Such improvement may be associated with the influence of the molecular additive in changing the crystallization dynamics (e.g., growth reaction rates, precursor diffusion rates, etc.) of the perovskite films (*30*). The detailed mechanism shall be explored in a separate study.

The post-deposition treatment by PEAI also improves the surface morphology of the perovskite film (Fig. 2C) but does not appear to further enhance its crystallinity. The combination of the additive and surface treatments provides the most uniform and compact film morphology with vertically oriented grains (Fig. 2, C and D). Optical absorption and photoluminescence (PL) spectra of the modified samples were measured (Fig. 2B and fig. S3). The reduced Urbach energy (E_U) [extracted from the absorption spectra (*31*)] and enhanced PL intensity of the Cy + PEAI–treated perovskite film both point to substantially reduced trap states in the film.

To construct the inverted (p-i-n) PV cell structure, we select nickel oxide (NiO_x) as the hole transport layer (*32*) and phenyl-C_{61}-butyric acid methyl ester ($PC_{61}BM$) as the electron transport layer. An ultrathin bathocuproine (BCP) spacer layer is evaporated on top of the PCBM layer before deposition of the top metal electrode to reduce exciton quenching and enhance V_{OC} (*33*). The typical current density–voltage (J-V) curves of the pristine and optimized devices are shown in Fig. 3A. It can be clearly seen that the combined Cy/PEAI treatment has enhanced the PV cell efficiency, raising the V_{OC} from 0.98 to 1.08 V under AM1.5G illumination.

The importance of the additive and surface modification becomes more pronounced at low light intensity, a regime that resembles the designated application scenarios of such photodetectors. Figure 3B displays the relationship of V_{OC} versus light intensity across a wide intensity range. Under the light intensity of 10^{-5} mW/cm^2, the perovskite treatment results in a 45% improvement of the V_{OC},

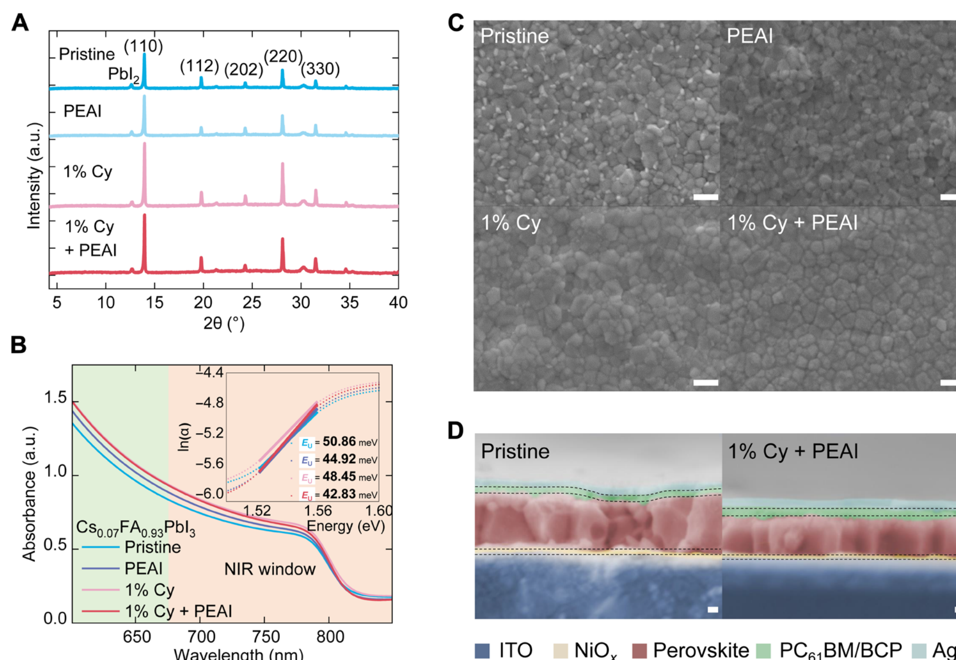

Fig. 2. Characterizations of perovskite films. (**A**) X-ray diffraction patterns of perovskite films based on NiO_x. a.u., arbitrary units. (**B**) Absorption spectra of perovskite films, with inset showing the Urbach energy. (**C**) Planar SEM images of perovskite films after different treatments, with scale bars indicating 5 μm. (**D**) Cross-sectional SEM images of perovskite films after different treatments, with scale bars indicating 100 nm and dashed lines indicating interfaces.

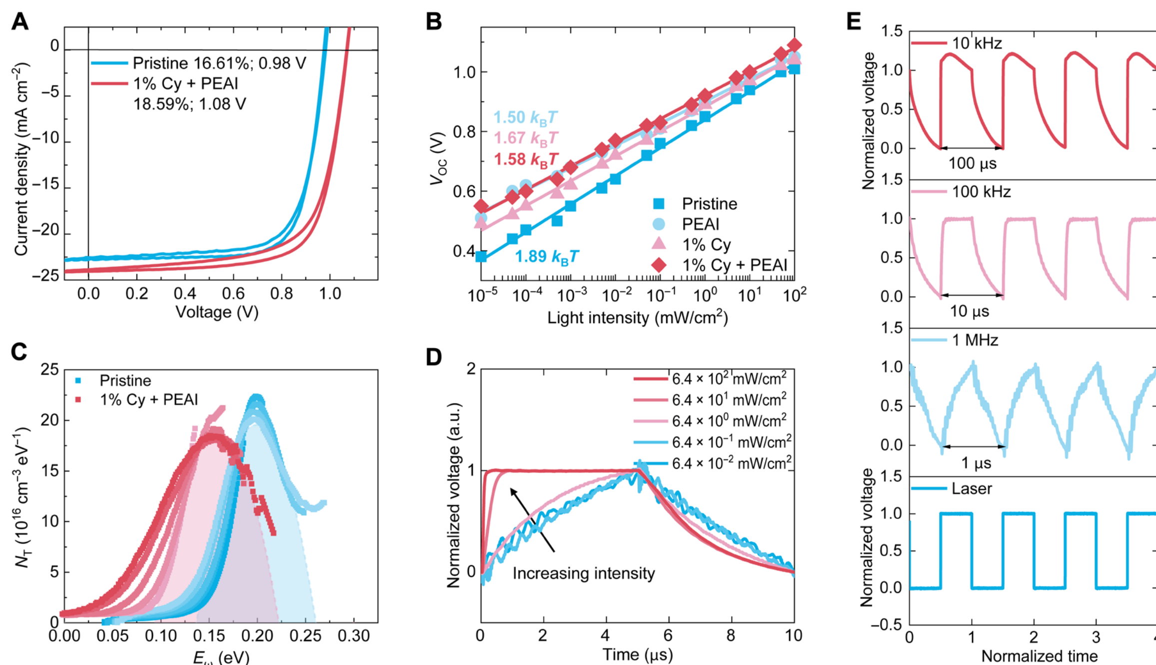

Fig. 3. Characterizations of PV cells. (**A**) The *J-V* curve of the pristine and optimized PV cell under one-sun (10^2 mW/cm^2) conditions. (**B**) V_{OC} versus light intensity for the PV cells with different treatments. (**C**) Defect energy distribution of pristine and optimized PV cells extracted by thermal admittance spectroscopy analysis. (**D**) Transient voltage response of the optimized PV cell in open circuit under a different light intensity (λ = 635 nm, 100 kHz). (**E**) Transient voltage response of the optimized PV cell in open circuit under 6.4×10^1 mW/cm^2 illumination (λ = 635 nm) and a different frequency.

increasing its value from 0.38 to 0.55 V. The ideality factor (n_{ID}) extracted from the slope of the lines is between 1 and 2, confirming that the dominant recombination mechanism at the weak light regime is trap-assisted recombination (*34*). The recombination rates K_r extracted from the transient photovoltage response are shown in fig. S5. As expected, K_r is reduced after the recombination pathways are partially eliminated via defect passivation. The time-resolved PL result also shows that the optimized sample has a longer carrier lifetime (fig. S6D). The increased time constants of both the fast (12.8 to 63.7 ns) and slow (142.1 to 228.1 ns) decay components indicate the suppression of trap-assisted recombination in both the bulk and surface of the perovskite films (*35*). Last, the trap states in PV cells are analyzed quantitatively with thermal admittance spectroscopy (Fig. 3C and fig. S7). It can be clearly observed in Fig. 3C that the surface and additive modifications have reduced both the trap depth and trap density.

Next, we evaluate the photovoltage response speed of the PV cell. Because short-channel IGZO FETs generally exhibit fast switching speed due to their high field-effect mobility (*36*), the operation speed of the PVT is limited by the temporal response of the PV module. The transient voltage response of the optimized PV cell is shown in Fig. 3 (D and E), exhibiting a fast rise time τ_r of 420 ns and a fall time τ_f of 3.3 μs even at a low light intensity of tens of milliwatts per square centimeter. The measured 3-dB bandwidth is about 0.4 MHz (fig. S6). Note that these results were obtained at open circuit. We also measured the transient current response at short circuit (fig. S6) under the same light excitation condition and obtained a reduced τ_r of 348 ns, a τ_f of 332 ns, and an f_{3dB} of 1.9 MHz due to rapid charge recombination through the external circuit. In the PVT structure, the PV module is close to the open-circuit condition, but charge recombination could be assisted by the positively biased control gate and the small leakage current through the dielectric layer. As a result, it is expected that the 3-dB bandwidth of the PVT will lie in between the $f_{3dB_open\text{-}circuit}$ and $f_{3dB_short\text{-}circuit}$ of the corresponding PV cell under the same light excitation.

Integration and characterization of PVT photodetectors

Because the electrical amplification of the PVT relies on the transconductance g_m of the IGZO FET, we designed a large W/L ratio of 840 (W = 25,200 μm and L = 30 μm) for the source and drain electrodes of the transistor. The optical images of the IGZO FETs are shown in fig. S8 (A and B), and the transfer and output characteristics of the device are plotted in Fig. 4A and fig. S8D, respectively. Notably, the IGZO transistor module is highly transparent (fig. S8C), thus allowing for efficient light penetration to the PV module. The extracted mobility is more than 10 cm^2/(V·s), and the subthreshold swing is around 400 mV/dec. The g_m (red line in Fig. 4A) reaches its maximum around a V_G of 3 V with a value of 5.38×10^{-4} S. The electrical gain can be tuned by V_G as shown in fig. S8E.

On the basis of the optimized PV cell and IGZO FET, we monolithically fabricated the PVT device (optical image shown in fig. S9A) through a layer-by-layer fashion as described in Materials and Methods. The threshold voltage (V_{th}) of the PVT is 0.73 V, slightly higher than the V_{th} of 0.70 V for the pure FET, which is probably caused by the annealing step during the fabrication of PV cells. The performance of the PV module in the PVT is characterized (fig. S9B). Although the fill factor of the device drops as compared to pure PV cells, due possibly to the low-powered sputtered ITO being less conductive than the commercial ITO coating, the V_{OC} of the PV module in the PVT remains almost the same as those obtained from pure PV cells.

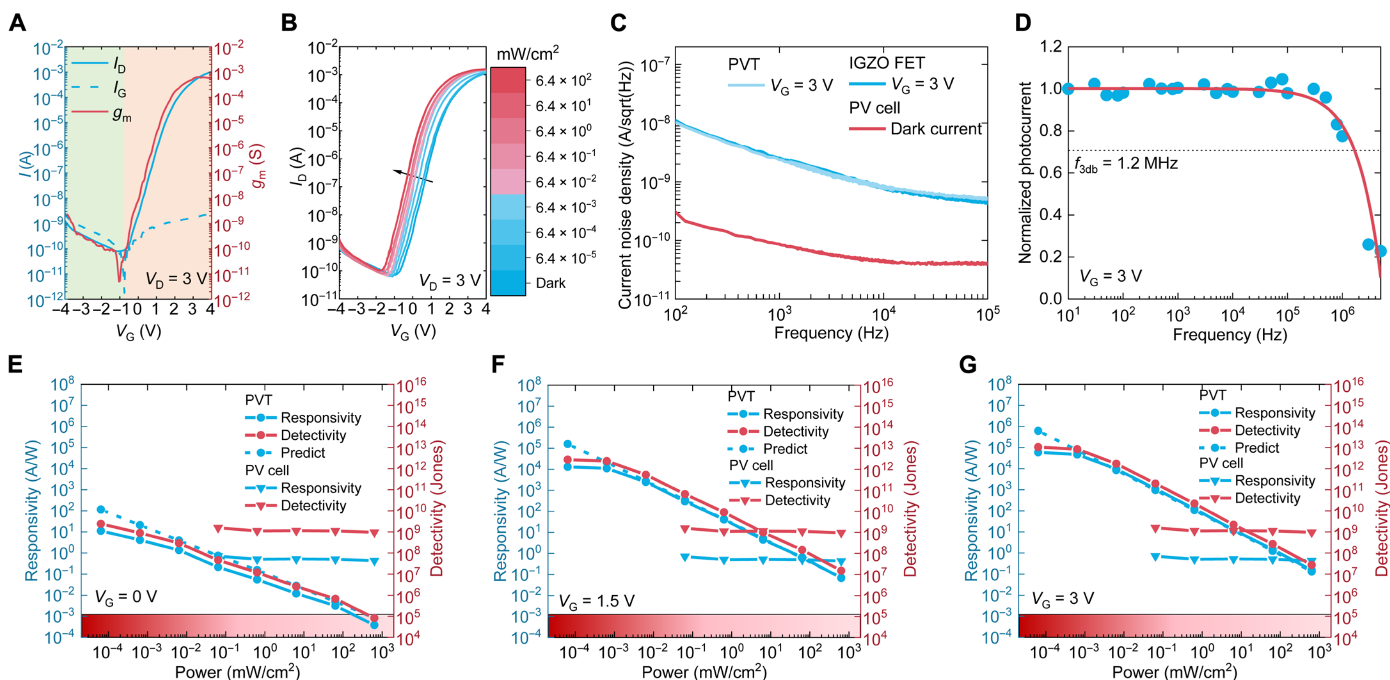

Fig. 4. Characterizations of PVTs. (**A**) Transfer characteristic of the IGZO FET when V_D = 3 V. (**B**) Photoresponse of the PVT under a different light intensity (λ = 635 nm, 100 kHz) when V_D = 3 V. (**C**) Noise current of the PVT, IGZO FET, and PV cell. (**D**) Frequency response of the PVT under 6.4×10^1 mW/cm^2 illumination (λ = 635 nm) when V_G = 3 V. (**E** to **G**) Responsivity and detectivity of the PVT and PV cell under a different light intensity (λ = 635 nm) and gate bias.

The photoresponse of the PVT is shown in Fig. 4B. It can be seen that, with the increasing incident light intensity, the V_{th} negatively shifts while the off-current stays almost unchanged, suggesting that the anode of the PV module behaves as a float gate to the n-channel. This is in contrast with the photocurrent-based photodetectors, which show enhanced off-current upon illumination. The responsivity (R)–light intensity relation of the PVT is shown in Fig. 4 (E to G). Consistent with the theoretical model presented in the above section, under low light intensity, the signal of the PVT is logarithmically proportional to the number of photons. For comparison, we also plot the R of the PV cell working as a PD detector. The R of the PD barely changes with reduced light intensity, in accordance with Eq. 6 where $\gamma \sim 1$. By contrast, the R of PVT rises fast and outperforms PD. As illustrated by Eq. 4, the R value can be enhanced with a higher g_m by increasing the control gate voltage V_G. In Fig. 4F, when the g_m reaches its maximum ($V_G \sim 3$ V), the PVT can outperform the PD even at the one-sun condition. The data are well fit by Eq. 4 (dashed lines in Fig. 4, E to G) and validate the proposed theory except under very weak light intensity. This could be because the theory ignores the environmental light interference, under which the PV module readily generates a photovoltage and leads to a noticeable reduction in V_{th} shift compared to theoretical prediction. The EQE of the fabricated PVT device is shown in fig. S9D. It can be seen that the EQE spectrum of the PVT has a very similar shape as that of its PV module, except that the former is several orders of magnitude larger in amplitude, which confirms that the photoresponse of the PVT is controlled by the photocarrier generation in the PV module. A larger V_{OC} from the PV module is also beneficial for a higher R value (fig. S10).

Next, we characterize the specific detectivity D^* of the photodetector, which represents the minimum input optical power to generate detectable electrical output. To quantify $D^* = \frac{R\sqrt{A}}{I_n}$ (A is the illumination area and I_n is the noise current density), we carefully measured I_n in a shielding metal box (Faraday cage) to prevent external electromagnetic interference. Both the PVT and FET devices exhibit a typical frequency-dependent $1/f$ noise (Fig. 4C and fig. S9C). We note that contact resistance can also dominate the transistor noise in certain device configurations (*37*). In our current IGZO transistor configuration, the effect of the contact resistance is relatively small (fig. S8D). Moreover, the noise of the FET module is nearly one order of magnitude higher than that of the PV module, while the difference in the noise of the PVT and FET is almost negligible. This result suggests that the noise of the detector originates from the transistor module and can be further suppressed upon reduction of the trap states in the transistor (*38*, *39*).

The frequency responses of the PVT are displayed in Fig. 4D (for $V_G = 3$ V) and fig. S11 (for other voltage conditions). The f_{3dB} reaches 1.2 MHz at the on-state of the transistor, and, as expected, this value falls in between the $f_{3dB_open\text{-}circuit}$ and $f_{3dB_short\text{-}circuit}$ of the single PV cell under the same light excitation. Note that, here, we focus on the frequency limit of the PV module, because typically the gate delay of the transistor module (~10 ns for the IGZO FET) is much faster than that of the PV module (~3.3 μs for the PV cell). When other types of PV and transistor structures are used, the characteristics of the transistor module may also play a role in limiting the frequency of the PVT. For instance, the source and drain contact resistance of a FET, i.e., $R_s + R_d$, may also limit the high-frequency operation according to $f_{max,bd} \approx \frac{f_{T,bd}}{2\sqrt{(R_g + R_s + R_d)G_{ds} + 2\pi f_{T,bd} C_{gd} R_g}}$ (*40*). In our device, the effect of the contact resistance on the frequency is small (see detailed analysis in the Supplementary Materials).

Last, we compare the product of R and f_{3dB}, i.e., the gain-bandwidth product (GBP), of our devices and compare it with other types of photodetectors, including III-V and Si-based devices (Fig. 5). GBP is chosen as the figure of merit for comparison here, as it reflects how a photodetector is constrained from the gain-bandwidth trade-off. It has also been proposed as a critical parameter to evaluate photodetector performance (*41*, *42*). Here, we use gain and responsivity interchangeably, as photodetector gain scales linearly with responsivity. It can be clearly seen from the figure that PTs can achieve very high responsivity, but the response speed drops substantially at large R values, as described also by Eq. 5 ($R_{PT} \propto \tau_p$ but $f \propto 1/\tau_p$); accordingly, the data points of PT fall in the fourth quadrant of Fig. 5. On the other hand, some photoconductors and PDs exhibit a gigahertz bandwidth, but due to the lag of a gain mechanism, their R value is below 1 A/W, corresponding to the data points in the second quadrant of Fig. 5. The data points of the PVT structure fall in the first quadrant, displaying both high R and f_{3dB} (red stars in Fig. 5), agreeing with the characteristics predicted by Eq. 4, and the GBP could be generally expressed as $\text{GBP} = Rf \sim (g_m V_G V_{oc})/[P(\tau_{TFT} + \tau_p)]$. We note that the CQD/Si PVT also presents both high R and f_{3dB} (*7*), but its response speed is slower than our PVT due likely to the deep trap states of the CQDs limiting the response speed. The performance data distribution in Fig. 5 illustrates how the new PVT is able to surpass the benchmark in terms of R, f_{3dB}, and their GBP. The separation of the photoswitching (by the PV module) and gain (by the FET module) functions via the float gate and control gate, respectively, allows for further optimization of the device performances, i.e., responsivity, noise, and bandwidth, via engineering of separate active layers and device modules. Note also that, compared to magnifying the output of a PD with an amplifier circuit, a single PVT device achieves the amplification function while avoiding a substantial increase of the device footprint and eliminating the use

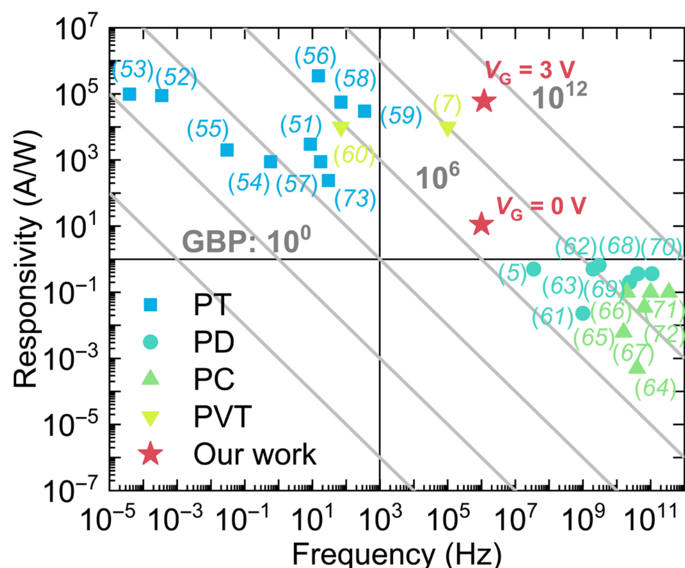

Fig. 5. Overview of performance metrics of various photodetectors. Data points of different photodetector structures plotted against their corresponding responsivity and a 3-dB bandwidth (*5*, *7*, *51*–*73*). Gray lines represent different GBP values. Data obtained from PVT (developed in this work) are represented by red stars.

of wire connections, which reduces the parasitic capacitance, resistance, and noise of the entire system.

Application of PVT in photoplethysmography

To demonstrate the benefit of high GBP in weak light applications (e.g., biomedical sensors), we exploit the PVT as the detection unit of a PPG sensor. PPG is a widely used optical approach to monitor vital health parameters such as heart pulsation, arterial blood pressure, and blood oxygen level (*43*). In a typical PPG sensor, a light-emitting diode (LED) is used to emit light to the skin tissue, and the portion of the tissue-absorbed light can be dynamically monitored by a photodetector placed either on the same side of the LED (to capture back-reflected/scattered light) or on the opposite side of the LED (to capture transmitted light). The variation of the detected signal reflects the systolic and diastolic processes in an arterial pulse wave (Fig. 6A). For wearable applications, the light intensity of the LED is typically kept low to minimize the power consumption of the device; hence, after tissue absorption and scattering, the detector unit of the PPG sensor only receives a very weak light signal.

Here, we used a reflection mode setup to measure the PPG signal on a fingertip (Fig. 6A). The intensity of the LED is varied to examine the signal quality under different illumination conditions. For comparison, a separate PPG sensor consisting of the same LED and a typical organic heterojunction-based ($P_3HT/PC_{61}BM$) PT as the detector is constructed. The PT has a responsivity comparable to that of the PVT under the same illumination (fig. S12). As shown in Fig. 6B, under high-power LED illumination, both sensors can collect waveforms with well-defined systolic and diastolic peaks. Occasionally, the diastolic peaks disappear in the organic PT-based PPG due to its slow response to light variation. However, when the LED power drops, a remarkable difference in the performance of the two sensors is observed: While the PVT can still reserve all the waveform features without distortion, the organic PT-based PPG has lost a substantial portion of the arterial waveform, as the slow response of the detector can no longer capture the dynamic change of the light absorption by the blood vessels. Notably, the signal fidelity of PPG is important to precisely extract the temporal variation of the systolic peaks to characterize the heart rate (*44*) and blood pressure (*45*) and that of the diastolic peaks (the second major peak) to estimate artery stiffness (*46*).

DISCUSSION

In conclusion, we provide a solution to the gain-bandwidth trade-off problem by developing a PVT structure, i.e., a monolithic integrated photodetector with the photovoltage cell introducing a float gate on a transistor. The optical gain and electrical gain could be separately optimized by enlarging V_{OC} in the PV module and increasing g_m in the FET module, respectively. In the meantime, the fast speed could also be obtained by minimizing the photovoltage cell delay τ_{PV} (i.e., removing deep traps) and the transistor gate delay τ_{TFT} (i.e., enlarging g_m). As such, the trade-off between gain and response speed (the bandwidth) could be addressed. The integrated PVT sets a new record for the GBP and demonstrates a high D^* of 1.06×10^{13} Jones at a small control gate voltage of 3 V. It also shows superior performance in detecting low light power PPG signals as compared to conventional detectors.

There is still great room for improvement of the PVT performance in terms of material choices and device structures. For instance, by reducing the trap density and contact resistance in the transistor channel, the noise current of the PVT can be largely suppressed. The responsivity of the PVT can be enhanced by reducing the channel length and using high-*k* materials for the gate dielectric layer. The spectral response and photovoltage modulation can be done via selection and optimization of the photoactive material. In terms of fabrication, one can reduce the number of layers in the PV module by building a simple Schottky junction at the photoactive layer/float gate interface for photovoltage generation, thus reducing the processing steps. In addition to the perovskite–metal oxide combination, many other material combinations can be explored. For example, organic semiconductors are known to provide highly tunable electronic properties. All-organic PVTs can be made through rapid vacuum deposition processes or even inkjet printing, if orthogonal solvents for multilayer deposition can be identified. Last but not the

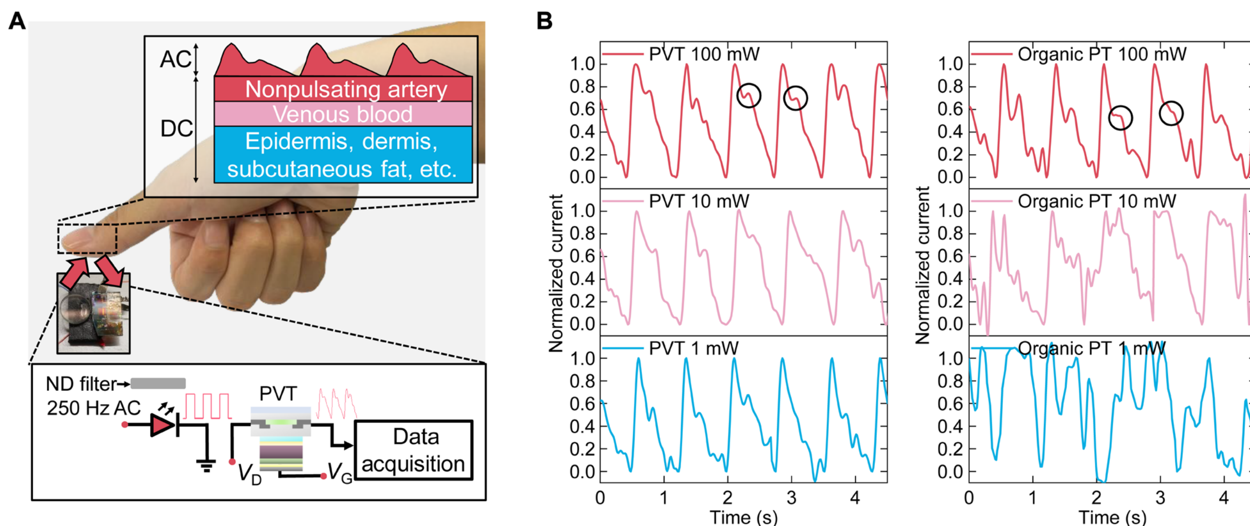

Fig. 6. Photoplethysmography measurement using PVT. (**A**) Schematic of electrical circuits and the working principle of PPG. (**B**) PPG signal collected by PVT and organic PT under different light intensities. The circles highlight the diacritic notches resolvable from the waveforms.

least, new functions, such as narrow-band detection and x-ray detection, can also be explored on the basis of the PVT mechanism.

MATERIALS AND METHODS

Fabrication of perovskite solar cell

A schematic illustration of the fabrication process is shown in fig. S13B. The ITO-coated glass was ultrasonically cleaned with cleaning fluid, deionized (DI) water, acetone, isopropyl alcohol (IPA), and ethanol for 10 min, respectively. Before the deposition of the NiO_x layer, ITO substrates were cleaned by ultraviolet/ozone for 30 min. The NiO_x layer was deposited by spin coating precursor solutions of Li-doped NiO (LiNiO) at 6000 rpm for 30 s. The NiO_x film was heated at 100°C for 10 min and 230°C for 1 hour in the air. The LiNiO precursor solution was prepared by dissolving 87 mg of $Ni(NO_3)_2$ (Sigma-Aldrich), 28 mg of LiAc (Sigma-Aldrich), and 23 mg of CH_4N_2S (Sigma-Aldrich) in 2 ml of DI water and was stirred overnight. Twenty-four microliters of $FAPbI_3$ [1.26 M PbI_2, Tokyo Chemical Industry (TCI) Development; 1.08 M formamidinium iodide (FAI), Greatcell Solar Materials; *N*,*N*′-dimethylformamide:dimethyl sulfoxide (DMF:DMSO) = 4:1, v/v], to which 5 volume % CsI (1.5 M in DMSO; Alfa Aesar) and 1% Cy (Greatcell Solar Materials) relative to PbI_2 were added, was spun on the NiO_x layer at 1000 rpm for 10 s and 6000 rpm for 20 s in a glovebox with N_2 atmosphere. The antisolvent of chlorobenzene (CB) was dripped at the 20th second. The resulting film was annealed at 110°C for 40 min. Afterward, 10 μl of PEAI (Greatcell Solar Materials) salt solution [5 mM in IPA with 1% DMF and FAI (1 mg/ml)] was spin-coated onto the perovskite layer at 3000 rpm for 30 s. Additional DMF can dissolve the top perovskite and recrystallize with PEAI (*47*) to generate a uniform distribution of perovskite and passivators. The SEM images are shown in Fig. 2C and fig. S2B, confirming the smoothened surface. The new devices exhibit improved performance (fig. S3C) including short-circuit current I_{SC} (fig. S4B). V_{OC} also benefits because FAI may react with PbI_2 and function like a self-healer for the grain boundary just like methylammonium iodide (MAI) (*48*). Twenty-two microliters of $PC_{61}BM$ (Sigma-Aldrich) solution (20 mg/ml in CB) was spin-coated at 2000 rpm for 30 s. Thirty microliters of BCP (Sigma-Aldrich) solution (saturated in IPA) was spin-coated on the $PC_{61}BM$ layer at 1500 rpm for 30 s. Because the solution of BCP is IPA, which is corrosive to perovskite film, a dynamic spin-coating method should be adopted (*49*). Last, an Ag electrode (70 nm) was deposited by thermal evaporation under a high vacuum. The above processes were also carried out in a glovebox with N_2 atmosphere.

Fabrication of FETs

A schematic illustration of the fabrication process is shown in fig. S13C. The amorphous IGZO (a-IGZO) TFTs were fabricated on a glass substrate, which was cleaned with acetone, ethanol, and DI water. SiO_2 as a buffer layer to improve the surface morphology was deposited by plasma-enhanced chemical vapor deposition (PECVD) at 350°C with a mixed gas of silane and N_2O. A 40-nm-thick a-IGZO film was deposited at room temperature, using a sputter with O_2 and Ar, patterned by photolithography, and wet-etched by hydrochloric acid. The electrodes were fabricated by depositing a 60-nm-thick Mo layer. Gate insulator (SiO_2) was also deposited by PECVD at 180°C. The top gate (ITO) was fabricated by a sputter with Ar. The electrodes and top gate were defined by the lift-off process. Last, the devices were annealed at 350°C for 1.5 hours.

Fabrication of integrated PVT

The top electrode of the IGZO transistor was used to replace the ITO glass in the above PV cell fabrication steps. The electrode area of IGZO transistors was protected by tape during spin coating to prevent being short-circuited. The final device was encapsulated by a photosensitive resin to ensure stable operation in the air.

Characterizations

The transfer and output characterizations were conducted by a Keithley 4200 sourcemeter under dark conditions. For noise current spectral density, devices were powered by batteries and measured by a fast Fourier transform spectrum analyzer (SR760) in a metal shielding box after 5 min of stressing. For transient response, devices were powered by a Keithley 2612 sourcemeter and connected to an oscilloscope (Tektronix TDS3014C) via a high-speed current amplifier (Femto DHPCA-100). Laser (Newport LQA635) modulated with a function generator (Agilent 33210A) was chosen as the light source. The PPG signal was collected using a Keithley 2612 sourcemeter and controlled by a LabVIEW program on the computer.

Thermal admittance spectroscopy

The capacitance of samples is measured at various temperatures (T = 200 to 340 K) in the dark from 10^2 to 10^6 Hz (fig. S7, A and B). The DC bias is zero and the AC voltage is 30 mV during the measurement. The transition frequency is decided by taking the derivative of the capacitance spectra. The corresponding Arrhenius plots are plotted to calculate the activation energy E_a (fig. S7C). The Mott-Schottky analysis is carried out at a frequency of 1 kHz to extract built-in voltage V_{bi} and depletion width W_d (fig. S7D). Last, the energetic defect distribution is calculated using the equation (*50*)

$$N_T(E_\omega) = -\frac{V_{bi}}{q\,W_d}\frac{dC}{d\omega}\frac{\omega}{kT}$$

where C is the capacitance, ω is the frequency, T is the temperature, and E_ω is the converted energy from frequency.

SUPPLEMENTARY MATERIALS

Supplementary material for this article is available at https://science.org/doi/10.1126/sciadv.abq0187

REFERENCES AND NOTES

1. L. Gu, S. Poddar, Y. Lin, Z. Long, D. Zhang, Q. Zhang, L. Shu, X. Qiu, M. Kam, A. Javey, Z. Fan, A biomimetic eye with a hemispherical perovskite nanowire array retina. *Nature* **581**, 278–282 (2020).
2. C. Bao, J. Yang, S. Bai, W. Xu, Z. Yan, Q. Xu, J. Liu, W. Zhang, F. Gao, High performance and stable all-inorganic metal halide perovskite-based photodetectors for optical communication applications. *Adv. Mater.* **30**, e1803422 (2018).
3. P. C. Y. Chow, T. Someya, Organic photodetectors for next-generation wearable electronics. *Adv. Mater.* **32**, e1902045 (2020).
4. X. Zhou, X. Hu, B. Jin, J. Yu, K. Liu, H. Li, T. Zhai, Highly anisotropic GeSe nanosheets for phototransistors with ultrahigh photoresponsivity. *Adv. Sci.* **5**, 1800478 (2018).
5. R. Maiti, C. Patil, M. A. S. R. Saadi, T. Xie, J. G. Azadani, B. Uluutku, R. Amin, A. F. Briggs, M. Miscuglio, D. Van Thourhout, S. D. Solares, T. Low, R. Agarwal, S. R. Bank, V. J. Sorger, Strain-engineered high-responsivity $MoTe_2$ photodetector for silicon photonic integrated circuits. *Nat. Photonics* **14**, 578–584 (2020).
6. C. T. Liu, S. Luryi, Photovoltaic transistors based on a steady-state internal polarization effect in asymmetric semiconductor superlattices. *Appl. Phys. Lett.* **59**, 393–395 (1991).
7. V. Adinolfi, E. H. Sargent, Photovoltage field-effect transistors. *Nature* **542**, 324–327 (2017).
8. B. Xiang, T. Zou, Y. Wang, C. Liu, J. Chen, K. Wang, Q. Dai, S. Zhang, H. Zhou, Photovoltage-coupled dual-gate InGaZnO thin-film transistors operated at the subthreshold region for low-power photodetection. *ACS Appl. Electron. Mater* **2**, 1745–1751 (2020).

9. T. Kamiya, K. Nomura, H. Hosono, Present status of amorphous In-Ga-Zn-O thin-film transistors. *Sci. Technol. Adv. Mater.* **11**, 044305 (2010).
10. M. M. Billah, A. B. Siddik, J. B. Kim, D. K. Yim, S. Y. Choi, J. Liu, D. Severin, M. Hanika, M. Bender, J. Jang, High-performance coplanar dual-channel a-InGaZnO/a-InZnO semiconductor thin-film transistors with high field-effect mobility. *Adv. Electron. Mater.* **7**, 2000896 (2021).
11. J. Zhang, W. Huang, K. C. Chang, Y. Shi, C. Zhao, X. Wang, H. Meng, S. Zhang, M. Zhang, Performance enhancement and bending restoration for flexible amorphous indium gallium zinc oxide thin-film transistors by low-temperature supercritical dehydration treatment. *ACS Appl. Mater. Interfaces* **13**, 8584–8594 (2021).
12. Z. Li, T. R. Klein, D. H. Kim, M. Yang, J. J. Berry, M. F. A. M. van Hest, K. Zhu, Scalable fabrication of perovskite solar cells. *Nat. Rev. Mater.* **3**, 18017 (2018).
13. H. Min, D. Y. Lee, J. Kim, G. Kim, K. S. Lee, J. Kim, M. J. Paik, Y. K. Kim, K. S. Kim, M. G. Kim, T. J. Shin, S. Il Seok, Perovskite solar cells with atomically coherent interlayers on SnO_2 electrodes. *Nature* **598**, 444–450 (2021).
14. J. Zhou, J. Huang, Photodetectors based on organic-inorganic hybrid lead halide perovskites. *Adv. Sci.* **5**, 1700256 (2018).
15. M. A. Green, A. Ho-Baillie, H. J. Snaith, The emergence of perovskite solar cells. *Nat. Photonics* **8**, 506–514 (2014).
16. X. He, J. Chen, X. Ren, L. Zhang, Y. Liu, J. Feng, J. Fang, K. Zhao, S. F. Liu, 40.1% record low-light solar-cell efficiency by holistic trap-passivation using micrometer-thick perovskite film. *Adv. Mater.* **33**, e2100770 (2021).
17. I. Raifuku, Y. Ishikawa, S. Ito, Y. Uraoka, Characteristics of perovskite solar cells under low-illuminance conditions. *J. Phys. Chem.* **120**, 18986–18990 (2016).
18. M. Li, F. Igbari, Z. K. Wang, L. S. Liao, Indoor thin-film photovoltaics: Progress and challenges. *Adv. Energy Mater.* **10**, 2000641 (2020).
19. C. L. Cutting, M. Bag, D. Venkataraman, Indoor light recycling: A new home for organic photovoltaics. *J. Mater. Chem. C* **4**, 10367–10370 (2016).
20. M. M. Furchi, A. Pospischil, F. Libisch, J. Burgdorfer, T. Mueller, Photovoltaic effect in an electrically tunable van der Waals heterojunction. *Nano Lett.* **14**, 4785–4791 (2014).
21. Y. Dan, X. Zhao, K. Chen, A. Mesli, A photoconductor intrinsically has no gain. *ACS Photonics* **5**, 4111–4116 (2018).
22. M. Marinkovic, D. Belaineh, V. Wagner, D. Knipp, On the origin of contact resistances of organic thin film transistors. *Adv. Mater.* **24**, 4005–4009 (2012).
23. A. Risteska, K. Myny, S. Steudel, M. Nakamura, D. Knipp, Scaling limits of organic digital circuits. *Org. Electron.* **15**, 461–469 (2014).
24. H. Klauk, Will we see gigahertz organic transistors? *Adv. Electron. Mater.* **4**, 1700474 (2018).
25. Y. Xu, Q. Lin, Photodetectors based on solution-processable semiconductors: Recent advances and perspectives. *Appl. Phys. Rev.* **7**, 011315 (2020).
26. J. Chen, N.-G. Park, Causes and solutions of recombination in perovskite solar cells. *Adv. Mater.* **31**, e1803019 (2019).
27. J. Jeong, H. Kim, Y. J. Yoon, B. Walker, S. Song, J. Heo, S. Y. Park, J. W. Kim, G.-H. Kim, J. Y. Kim, Formamidinium-based planar heterojunction perovskite solar cells with alkali carbonate-doped zinc oxide layer. *RSC Adv.* **8**, 24110–24115 (2018).
28. F. Xie, C.-C. Chen, Y. Wu, X. Li, M. Cai, X. Liu, X. Yang, L. Han, Vertical recrystallization for highly efficient and stable formamidinium-based inverted-structure perovskite solar cells. *Energ. Environ. Sci.* **10**, 1942–1949 (2017).
29. S. Zhang, G. Lanty, J.-S. Lauret, E. Deleporte, P. Audebert, L. Galmiche, Synthesis and optical properties of novel organic-inorganic hybrid nanolayer structure semiconductors. *Acta Mater.* **57**, 3301–3309 (2009).
30. A. Z. Chen, M. Shiu, X. Deng, M. Mahmoud, D. Zhang, B. J. Foley, S.-H. Lee, G. Giri, J. J. Choi, Understanding the formation of vertical orientation in two-dimensional metal halide perovskite thin films. *Chem. Mater.* **31**, 1336–1343 (2019).
31. A. Ajmi, K. Karoui, K. Khirouni, A. Ben Rhaiem, Optical and dielectric properties of $NaCoPO_4$ in the three phases α, β and γ. *RSC Adv.* **9**, 14772–14781 (2019).
32. F. Ma, Y. Zhao, J. Li, X. Zhang, H. Gu, J. You, Nickel oxide for inverted structure perovskite solar cells. *J. Energy Chem.* **52**, 393–411 (2021).
33. C. Chen, S. Zhang, S. Wu, W. Zhang, H. Zhu, Z. Xiong, Y. Zhang, W. Chen, Effect of BCP buffer layer on eliminating charge accumulation for high performance of inverted perovskite solar cells. *RSC Adv.* **7**, 35819–35826 (2017).
34. W. Tress, M. Yavari, K. Domanski, P. Yadav, B. Niesen, J. P. Correa Baena, A. Hagfeldt, M. Graetzel, Interpretation and evolution of open-circuit voltage, recombination, ideality factor and subgap defect states during reversible light-soaking and irreversible degradation of perovskite solar cells. *Energ. Environ. Sci.* **11**, 151–165 (2018).
35. D. Shi, V. Adinolfi, R. Comin, M. Yuan, E. Alarousu, A. Buin, Y. Chen, S. Hoogland, A. Rothenberger, K. Katsiev, Low trap-state density and long carrier diffusion in organolead trihalide perovskite single crystals. *Science* **347**, 519–522 (2015).
36. K. Myny, The development of flexible integrated circuits based on thin-film transistors. *Nat. Electron.* **1**, 30–39 (2018).
37. P. Karnatak, T. P. Sai, S. Goswami, S. Ghatak, S. Kaushal, A. Ghosh, Current crowding mediated large contact noise in graphene field-effect transistors. *Nat. Commun.* **7**, 13703 (2016).
38. W. E. Muhea, T. Gneiting, B. Iñiguez, Current-voltage and flicker noise analysis and unified modeling for amorphous indium-gallium-zinc-oxide thin film transistors with etch stop layer from 298 to 333 K. *J. Appl. Phys.* **125**, 144502 (2019).
39. G. Zhou, S. Zhou, Q. Zhu, N. Zhao, Improving operational stability of p-type field-effect transistors by charge selective electrodes: A general strategy. *Adv. Electron. Mater.* **5**, 1900055 (2019).
40. D. Zhong, H. Shi, L. Ding, C. Zhao, J. Liu, J. Zhou, Z. Zhang, L. M. Peng, Carbon nanotube film-based radio frequency transistors with maximum oscillation frequency above 100 GHz. *ACS Appl. Mater. Interfaces* **11**, 42496–42503 (2019).
41. A. R. Hawkins, W. Wu, P. Abraham, K. Streubel, J. E. Bowers, High gain-bandwidth-product silicon heterointerface photodetector. *Appl. Phys. Lett.* **70**, 303–305 (1997).
42. V. J. Sorger, R. Maiti, Roadmap for gain-bandwidth-product enhanced photodetectors: Opinion. *Opt. Mater. Express* **10**, 2192–2200 (2020).
43. H. Xu, J. Liu, J. Zhang, G. Zhou, N. Luo, N. Zhao, Flexible organic/inorganic hybrid near-infrared photoplethysmogram sensor for cardiovascular monitoring. *Adv. Mater.* **29**, 1700975 (2017).
44. J. Allen, Photoplethysmography and its application in clinical physiological measurement. *Physiol. Meas.* **28**, R1–R39 (2007).
45. S. Haddad, A. Boukhayma, A. Caizzone, Continuous PPG-based blood pressure monitoring using multi-linear regression. *IEEE J. Biomed. Health Inform.* **26**, 2096–2105 (2021).
46. M. Elgendi, On the analysis of fingertip photoplethysmogram signals. *Curr. Cardiol. Rev.* **8**, 14–25 (2012).
47. L. Zhou, Z. Lin, Z. Ning, T. Li, X. Guo, J. Ma, J. Su, C. Zhang, J. Zhang, S. Liu, J. Chang, Y. Hao, Highly efficient and stable planar perovskite solar cells with modulated diffusion passivation toward high power conversion efficiency and ultrahigh fill factor. *Solar RRL* **3**, 1970111 (2019).
48. D.-Y. Son, J.-W. Lee, Y. J. Choi, I.-H. Jang, S. Lee, P. J. Yoo, H. Shin, N. Ahn, M. Choi, D. Kim, N.-G. Park, Self-formed grain boundary healing layer for highly efficient $CH_3NH_3PbI_3$ perovskite solar cells. *Nat. Energy* **1**, 16081 (2016).
49. T. Wu, Y. Wang, Z. Dai, D. Cui, T. Wang, X. Meng, E. Bi, X. Yang, L. Han, Efficient and stable $CsPbI_3$ solar cells via regulating lattice distortion with surface organic terminal groups. *Adv. Mater.* **31**, e1900605 (2019).
50. H. S. Duan, H. Zhou, Q. Chen, P. Sun, S. Luo, T. B. Song, B. Bob, Y. Yang, The identification and characterization of defect states in hybrid organic-inorganic perovskite photovoltaics. *Phys. Chem. Chem. Phys.* **17**, 112–116 (2015).
51. H. Xu, J. Li, B. H. Leung, C. C. Poon, B. S. Ong, Y. Zhang, N. Zhao, A high-sensitivity near-infrared phototransistor based on an organic bulk heterojunction. *Nanoscale* **5**, 11850–11855 (2013).
52. E. Liu, M. Long, J. Zeng, W. Luo, Y. Wang, Y. Pan, W. Zhou, B. Wang, W. Hu, Z. Ni, Y. You, X. Zhang, S. Qin, Y. Shi, K. Watanabe, T. Taniguchi, H. Yuan, H. Y. Hwang, Y. Cui, F. Miao, D. Xing, High responsivity phototransistors based on few-layer ReS_2 for weak signal detection. *Adv. Funct. Mater.* **26**, 1938–1944 (2016).
53. J. O. Island, S. I. Blanter, M. Buscema, H. S. van der Zant, A. Castellanos-Gomez, Gate controlled photocurrent generation mechanisms in high-gain In_2Se_3 phototransistors. *Nano Lett.* **15**, 7853–7858 (2015).
54. O. Lopez-Sanchez, D. Lembke, M. Kayci, A. Radenovic, A. Kis, Ultrasensitive photodetectors based on monolayer MoS_2. *Nat. Nanotechnol.* **8**, 497–501 (2013).
55. J. F. Gonzalez Marin, D. Unuchek, K. Watanabe, T. Taniguchi, A. Kis, MoS_2 photodetectors integrated with photonic circuits. *2D Mater. Appl.* **3**, 14 (2019).
56. W. Zhang, M.-H. Chiu, C.-H. Chen, W. Chen, L.-J. Li, A. T. S. Wee, Role of metal contacts in high-performance phototransistors based on WSe_2 monolayers. *ACS Nano* **8**, 8653–8661 (2014).
57. N. Huo, S. Yang, Z. Wei, S. S. Li, J. B. Xia, J. Li, Photoresponsive and gas sensing field-effect transistors based on multilayer WS_2 nanoflakes. *Sci. Rep.* **4**, 5209 (2014).
58. W. Feng, J.-B. Wu, X. Li, W. Zheng, X. Zhou, K. Xiao, W. Cao, B. Yang, J.-C. Idrobo, L. Basile, W. Tian, P. Tan, P. Hu, Ultrahigh photo-responsivity and detectivity in multilayer InSe nanosheets phototransistors with broadband response. *J. Mater. Chem. C* **3**, 7022–7028 (2015).
59. G. W. Mudd, S. A. Svatek, L. Hague, O. Makarovsky, Z. R. Kudrynskyi, C. J. Mellor, P. H. Beton, L. Eaves, K. S. Novoselov, Z. D. Kovalyuk, E. E. Vdovin, A. J. Marsden, N. R. Wilson, A. Patane, High broad-band photoresponsivity of mechanically formed InSe-graphene van der Waals heterostructures. *Adv. Mater.* **27**, 3760–3766 (2015).
60. Z. Yang, B. Jiang, Z. Zhang, Z. Wang, X. He, D. Wan, X. Zou, X. Liu, L. Liao, F. Shan, The photovoltaic and photoconductive photodetector based on GeSe/2D semiconductor van der Waals heterostructure. *Appl. Phys. Lett.* **116**, 141101 (2020).
61. P. Ma, N. Flöry, Y. Salamin, B. Baeuerle, A. Emboras, A. Josten, T. Taniguchi, K. Watanabe, L. Novotny, J. Leuthold, Fast $MoTe_2$ waveguide photodetector with high sensitivity at telecommunication wavelengths. *ACS Photonics* **5**, 1846–1852 (2018).

62. N. Youngblood, C. Chen, S. J. Koester, M. Li, Waveguide-integrated black phosphorus photodetector with high responsivity and low dark current. *Nat. Photonics* **9**, 247–252 (2015).
63. Thor Labs product DETO25A (2013); www.thorlabs.com.
64. F. Xia, T. Mueller, Y. M. Lin, A. Valdes-Garcia, P. Avouris, Ultrafast graphene photodetector. *Nat. Nanotechnol.* **4**, 839–843 (2009).
65. T. Mueller, F. Xia, P. Avouris, Graphene photodetectors for high-speed optical communications. *Nat. Photonics* **4**, 297–301 (2010).
66. X. Gan, R.-J. Shiue, Y. Gao, I. Meric, T. F. Heinz, K. Shepard, J. Hone, S. Assefa, D. Englund, Chip-integrated ultrafast graphene photodetector with high responsivity. *Nat. Photonics* **7**, 883–887 (2013).
67. S. Schuler, D. Schall, D. Neumaier, L. Dobusch, O. Bethge, B. Schwarz, M. Krall, T. Mueller, Controlled generation of a p-n junction in a waveguide integrated graphene photodetector. *Nano Lett.* **16**, 7107–7112 (2016).
68. R. J. Shiue, Y. Gao, Y. Wang, C. Peng, A. D. Robertson, D. K. Efetov, S. Assefa, F. H. Koppens, J. Hone, D. Englund, High-responsivity graphene-boron nitride photodetector and autocorrelator in a silicon photonic integrated circuit. *Nano Lett.* **15**, 7288–7293 (2015).
69. N. Flory, P. Ma, Y. Salamin, A. Emboras, T. Taniguchi, K. Watanabe, J. Leuthold, L. Novotny, Waveguide-integrated van der Waals heterostructure photodetector at telecom wavelengths with high speed and high responsivity. *Nat. Nanotechnol.* **15**, 118–124 (2020).
70. Y. Ding, Z. Cheng, X. Zhu, K. Yvind, J. Dong, M. Galili, H. Hu, N. A. Mortensen, S. Xiao, L. K. Oxenløwe, Ultra-compact integrated graphene plasmonic photodetector with bandwidth above 110 GHz. *Nanophotonics* **9**, 317–325 (2020).
71. Y. Salamin, P. Ma, B. Baeuerle, A. Emboras, Y. Fedoryshyn, W. Heni, B. Cheng, A. Josten, J. Leuthold, 100 GHz plasmonic photodetector. *ACS Photonics* **5**, 3291–3297 (2018).
72. Y. Chen, S. Williamson, T. Brock, F. W. Smith, A. R. Calawa, 375-GHz-bandwidth photoconductive detector. *Appl. Phys. Lett.* **59**, 1984–1986 (1991).
73. J. Qiao, F. Feng, S. Song, T. Wang, M. Shen, G. Zhang, X. Yuan, M. G. Somekh, Perovskite quantum dot-Ta_2NiSe_5 mixed-dimensional van der Waals heterostructures for high-performance near-infrared photodetection. *Adv. Funct. Mater.* **23**, 2110706 (2021).
74. Y. Yamada, T. Nakamura, M. Endo, A. Wakamiya, Y. Kanemitsu, Photocarrier recombination dynamics in perovskite $CH_3NH_3PbI_3$ for solar cell applications. *J. Am. Chem. Soc.* **136**, 11610–11613 (2014).
75. R. Chau, S. Datta, M. Doczy, B. Doyle, B. Jin, J. Kavalieros, A. Majumdar, M. Metz, M. Radosavljevic, Benchmarking nanotechnology for high-performance and low-power logic transistor applications. *IEEE Trans. Nanotechnol.* **4**, 153–158 (2005).
76. C. Liu, T. Minari, Y. Xu, B.-r. Yang, H.-X. Chen, Q. Ke, X. Liu, H. C. Hsiao, C. Y. Lee, Y.-Y. Noh, Direct and quantitative understanding of the non-Ohmic contact resistance in organic and oxide thin-film transistors. *Org. Electron.* **27**, 253–258 (2015).
77. C. Liu, C. Chen, X. Li, S. Hu, C. Liu, K. Huang, F. Dai, B. Zhang, X. Liu, T. Minari, Y. Y. Noh, J. Chen, A general approach to probe dynamic operation and carrier mobility in field-effect transistors with nonuniform accumulation. *Adv. Funct. Mater.* **29**, 1901700 (2019).

Acknowledgments: We thank G. D. Zhou for the help with the noise measurement and Y. Q. Xiao for the help with the PPG measurement. **Funding:** This study was supported by the Hong Kong Research Grants Council General Research Fund 14209620 (N.Z.) and the National Natural Science Foundation of China 61922090 (C.L.). **Author contributions:** N.Z. and C.L. designed and directed the research. G.C. fabricated the IGZO FETs. Y.L. fabricated and characterized the PV cells and PVTs. S.Z. assisted the optimization and device characterizations of PV cells. Y.L., N.Z., and C.L. wrote the manuscript, with inputs from all authors. **Competing interests:** The authors declare that they have no competing interests. **Data and materials availability:** All data needed to evaluate the conclusions in the paper are present in the paper and/or the Supplementary Materials.

Submitted 14 March 2022
Accepted 5 August 2022
Published 23 September 2022
10.1126/sciadv.abq0187